

Rapid, 3D Chemical Profiling of Individual Atmospheric Aerosols with Stimulated Raman Scattering Microscopy

Jianpeng Ao, Yiqing Feng, Simin Wu, Tao Wang, Jiwei Ling, Liwu Zhang,* and Minbiao Ji*

Visualizing the 3D chemical profiles of individual aerosols is crucial to understand their formation and aging processes, yet remains technically challenging. Here, the first application of stimulated Raman scattering (SRS) microscopy on 3D chemical imaging of individual aerosols in a nondestructive manner is demonstrated. SRS is capable of mapping chemical components of aerosols at a speed four orders of magnitude faster than conventional spontaneous Raman microscopy. Spatially resolved distributions of nitrates and sulfates reveal the fine structures and different mixing states of atmospheric particles. Moreover, high-throughput quantifications of chemical compositions and particle size distributions are realized by large-area imaging and statistical analysis. Its high-speed and 3D chemical quantification capabilities promise SRS microscopy as a unique tool for studying the properties of single atmospheric particles, and ultimately their impacts on climate and human health.

inhaled particulate matter and acute adverse health effects.^[2] And noted that the impacts of aerosols on climate and health are found to be strongly related to the chemical mixing states of individual particles,^[3] which appear largely heterogeneous because of various formation and photochemical aging processes.^[4] Hence, imaging methods capable of spatially resolving chemical compositions of individual particles are of great significance to help in understanding the birth and fate of aerosols.

Various techniques have been applied to characterize single aerosol particles, including atomic force microscopy (AFM),^[5] scanning electron microscopy (SEM),^[6] transmission electron microscopy (TEM),^[7] vibrational spectroscopy,^[8] mass

spectrometry,^[9] and X-ray microanalysis.^[10] To obtain improved imaging-based chemical analysis, combined approaches of several techniques are more extended recently. The combination of aerosol time-of-flight mass spectrometry (ATOFMS) and TEM has been widely used to determine chemical composition and explore mixing state of individual aerosol particles.^[11] TEM coupled with energy-dispersive X-ray analysis (TEM/EDX) has a long application history to provide morphological and elemental analysis of single aerosol particles.^[12] However, access to interior structural and compositional information for single particles by these techniques still remains difficult. For instance, nanometer-scale secondary ion mass spectrometry (NanoSIMS) could characterize particles by lateral ion maps and depth-resolved ion distributions,^[9c] but fails to directly image interior structures for analysis. Similarly, scanning probe techniques such as AFM, SEM, or TEM allow to characterize the morphology of individual aerosol particles but lack the effective information on their 3D chemical compositions.^[13]


Raman spectroscopy, a non-destructive vibrational spectroscopic technique, has shown great potential in probing airborne particles and characterizing their chemical compositions.^[14] Confocal Raman microscopy has been applied to image lateral-resolved chemical distribution of mixed particles by acquiring Raman spectra pixel-by-pixel, but suffers from slow speed due to weak Raman response.^[15] To improve signal intensity, surface-enhanced Raman scattering (SERS) spectroscopy, and tip-enhanced Raman scattering (TERS) spectroscopy have been developed.^[13,16] However, their uneven enhancements and reliance on near-field effects limit the application on 3D chemical quantification of aerosols. In addition, spontaneous Raman scattering of atmospheric particles is susceptible to fluorescence backgrounds, and its weak scattering cross section

1. Introduction

Aerosol particles, especially PM_{2.5} and PM₁₀ (particulate matter with diameters smaller than 2.5 and 10 μm) are ubiquitous but essential constituents in the atmosphere. These particles scatter and absorb radiation as well as serve as cloud condensation and ice nuclei, consequently affecting the Earth's energy budget and contributing to global warming.^[1] Meanwhile, epidemiological researches have proven positive correlations between increased

J. Ao, S. Wu, J. Ling, Prof. M. Ji
State Key Laboratory of Surface Physics and Department of Physics
Multiscale Research Institute of Complex Systems
Academy for Engineering and Technology
Key Laboratory of Micro and Nano Photonic Structures
(Ministry of Education)
Fudan University
Shanghai 200433, China
E-mail: minbiaoj@fudan.edu.cn

Y. Feng, T. Wang, Prof. L. Zhang
Shanghai Key Laboratory of Atmospheric Particle Pollution
and Prevention
Department of Environmental Science and Engineering
Shanghai Institute of Pollution Control and Ecological Security
Fudan University
Shanghai 200092, China
E-mail: zhanglw@fudan.edu.cn

 The ORCID identification number(s) for the author(s) of this article can be found under <https://doi.org/10.1002/smt.d.201900600>.

© 2019 The Authors. Published by WILEY-VCH Verlag GmbH & Co. KGaA, Weinheim. This is an open access article under the terms of the Creative Commons Attribution License, which permits use, distribution and reproduction in any medium, provided the original work is properly cited.

DOI: 10.1002/smt.d.201900600

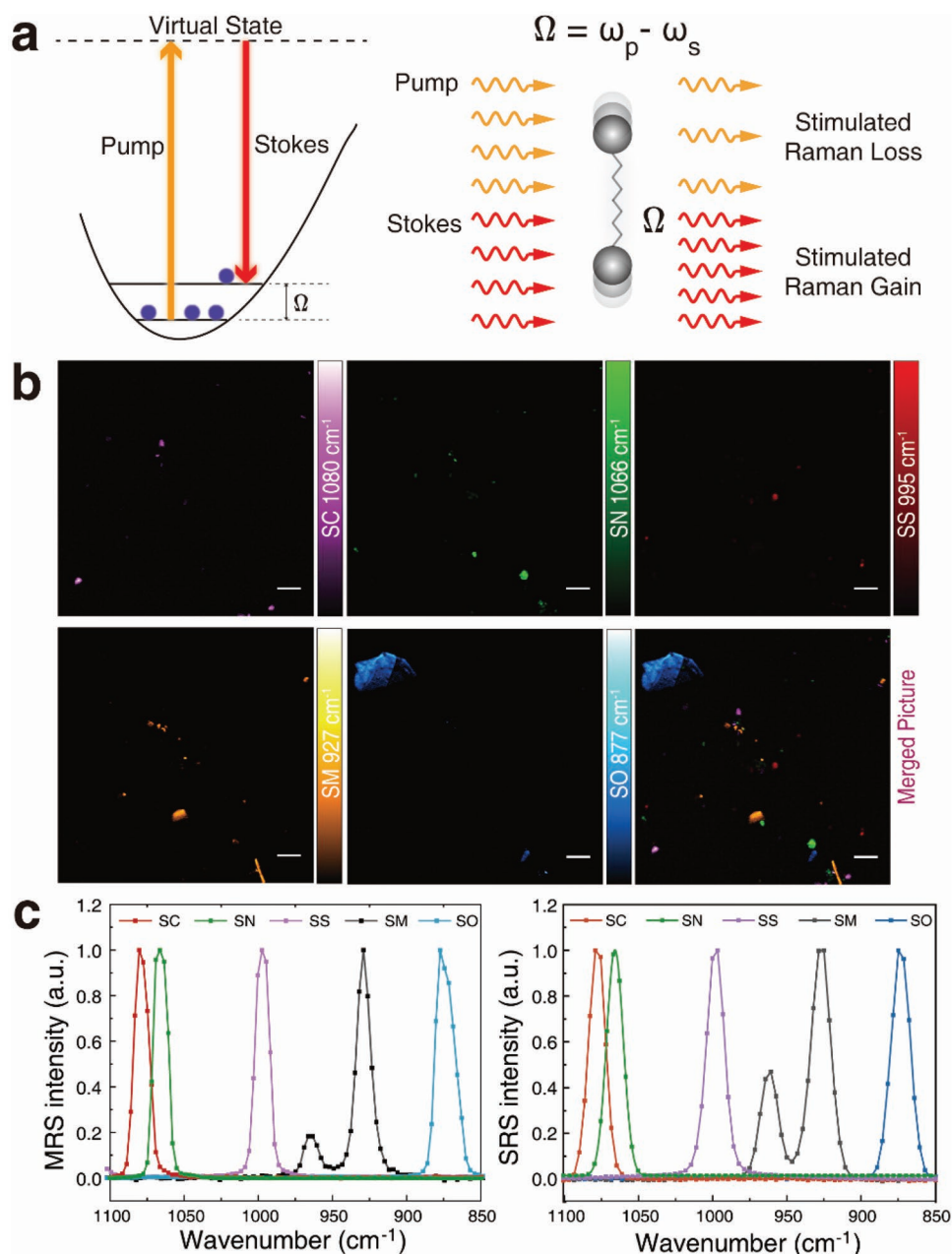


Figure 1. Characterization of SRS system. a) Energy diagram and photon conversions of SRS process. b) Chemical selective imaging of five standard compounds: SC (magenta), SN (green), SS (red), SM (orange), and SO (cyan) powders in a single FOV. c) The corresponding spontaneous and stimulated Raman scattering spectra of the five standard chemicals. Scale bar: 10 μm .

hinders high-speed imaging to characterize large amounts of particles efficiently.

Stimulated Raman scattering (SRS) is a coherent and nonlinear version of Raman scattering, gaining several orders-of-magnitude signal amplification while inheriting the spectroscopic nature of Raman scattering (Figure 1a).^[17] SRS microscopy is becoming a novel imaging technique with high chemical specificity and speed, showing great potentials mainly in biological and biomedical researches,^[18] with more recent demonstrations in material and earth sciences.^[19] In addition, SRS microscopy is capable of providing

high-resolution 3D images because of its optical nonlinearity similar to multiphoton microscopy.^[17a,20] Moreover, the linear dependence of SRS signal intensity on chemical concentration allows quantitative analysis and decomposition of mixed chemicals.^[18d,21] Given that the main chemical compositions of aerosol particles have distinct Raman features, SRS microscopy is expected to be a well-fitted technique for aerosol imaging, enabling both 3D characterization of single particles and high-throughput measurements for statistical analysis. However, to the best of our knowledge, no related work has been reported yet.

In this work, we demonstrated that SRS microscopy could serve as an ideal tool for characterizing aerosol particles. First of all, SRS provided chemical selective images at a speed four orders of magnitude faster than conventional micro-Raman spectroscopy (MRS) with higher spatial resolution. Second, 3D SRS imaging of individual aerosol particles successfully revealed the mixing states of different chemical components. Moreover, the capability of quantitative analysis was demonstrated by correlating the results of SRS large-area imaging with ion chromatography (IC), via measuring the mean mass ratios of NO_3^- and SO_4^{2-} (cited as N/S) from large amounts of aerosols. This high-throughput method also enabled statistical analysis such as particle size distributions. In addition, we studied ambient aerosol samples with SRS 3D chemical imaging and quantification at the single-particle level. These results indicated that SRS microscopy is a unique method for studying the chemical compositions and mixing structures of atmospheric aerosol particles, which may provide new insights to the formation and growth mechanisms of individual particles.

2. Results

2.1. Hyperspectral SRS Characterization of Major Chemical Components

The optical setup of SRS microscopy system is illustrated in Figure S1a (Supporting Information) and described with details in Note S1 (Supporting Information) and the Experimental Section. Throughout this work, we utilized the “spectral focusing” technique to achieve SRS frequency tuning by scanning the time delay between the chirped pump and Stokes pulses centered at 945 and 1040 nm, respectively, reaching $\approx 13 \text{ cm}^{-1}$ spectral resolution (Figure S1b–d, Supporting Information). In this way, the SRS spectra cover a range of 850 to 1100 cm^{-1} without adjusting

the laser wavelength. Differential transmission intensity (ΔI) of the pump beam with and without the Stokes was measured as the SRS signal (Figure 1a and Figure S1a, Supporting Information), and taken to generate SRS images pixel by pixel as the focused laser spot raster scanned across the samples. We first characterized the SRS spectra of five standard materials: sodium carbonate (Na_2CO_3 , SC), sodium nitrate (NaNO_3 , SN), sodium sulfate (Na_2SO_4 , SS), sodium malonate ($\text{C}_3\text{H}_2\text{O}_4\text{Na}_2$, SM), and sodium oxalate ($\text{Na}_2\text{C}_2\text{O}_4$, SO). The mixed powder of the five chemicals was imaged with hyperspectral SRS microscopy within the same field of view (FOV), generating a stack of images, each of which represented an SRS image at a particular Raman frequency. As shown in Figure 1b, the five components could be readily captured at their distinct Raman frequencies, showing clear vibrational resonances of the anions with Raman transitions. The extracted SRS spectra of these chemicals agree perfectly well with the corresponding spontaneous Raman spectra, as shown in Figure 1c. These results prove that SRS microscopy produces the spectral fingerprints of the compositions of particles to perform chemical imaging with high selectivity. It is worth mentioning that the organic components of aerosols are much more diverse and is not the main focus of the current work. Nevertheless, we showed trials of SRS characterization of secondary organic aerosol (SOA) ranging 1500 to 1750 cm^{-1} in Figure S2 (Supporting Information).

2.2. Rapid SRS Imaging of Typical Aerosols

Nitrates and sulfates are the two dominant inorganic components in ambient aerosols with strong Raman active modes of ν_s (SO_4^{2-} , 960–1005 cm^{-1}) and ν_1 (NO_3^- , 1045–1085 cm^{-1}).^[14c,15b] We synthesized aerosols with mixed nitrate and sulfate, and imaged them with both MRS and SRS within the same sample area, as shown in Figure 2. Although relatively higher laser

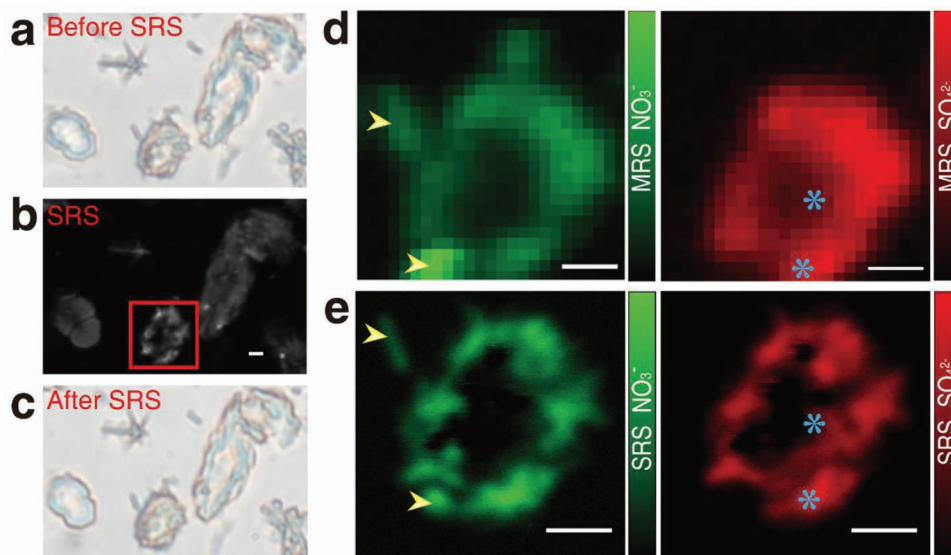


Figure 2. Stimulated versus spontaneous Raman scattering microscopy. a) Bright field image of typical aerosol particles before SRS. b) SRS image of the same FOV. c) Bright field image after SRS imaging. d) Micro-Raman and e) SRS images of an aerosol particle marked in (b), with the distribution of NO_3^- (green) and SO_4^{2-} (red); yellow arrow heads and blue stars indicate corresponding features between the two imaging modalities. Scale bar: 2 μm .

power was used in SRS (≈ 30 mW of Stokes and ≈ 20 mW of pump), no obvious photo-damage could be seen from the bright field images before and after SRS measurements (Figure 2a–c). We carefully examined a randomly picked particle within the FOV (red rectangle in Figure 2b). The distributions of NO_3^- and SO_4^{2-} were extracted from the MRS spectra pixel by pixel and shown in Figure 2d, whereas the same information was directly mapped with SRS microscopy from the two corresponding Raman frequencies, as shown in Figure 2e. The overall spatial profiles of each chemical composition appear roughly the same between MRS and SRS images. However, SRS clearly shows several advantages over MRS in terms of chemical imaging. First, SRS has much faster imaging speed: a 30×30 pixels MRS image takes ≈ 2.5 h, whereas a two-color SRS image of 512×512 pixels costs ≈ 2 s, achieving ≈ 4500 times increase of frame imaging speed. Second, SRS has higher spatial resolution: the commercial MRS system has a resolution of $\approx 1 \mu\text{m}$, whereas our homebuilt SRS microscope reaches ≈ 350 nm lateral resolution. As shown in Figure 2d, while the finer microstructures of both NO_3^- and SO_4^{2-} appear vague in MRS, they could be clearly seen with SRS (arrows and stars). In this particular aerosol particle with mixed compositions, although most of the structures contained overlapping NO_3^- and SO_4^{2-} , subtle differences between them could be uncovered by SRS (arrows and stars, Figure 2e). The ability of SRS microscopy to selectively image each chemical composition with high speed and resolution is crucial for aerosol particle studies.

2.3. 3D Chemical Imaging of Single Aerosol Particles

SRS is a third-order nonlinear optical process with signal intensity proportional to the product of the pump and Stokes laser power intensities. Such a nonlinearity results in the intrinsic optical sectioning capability, similar to two-photon fluorescence microscope, where the signal predominantly generates from the tight focus.^[20] By stepping through the z-axis of the samples with a step size of $0.4 \mu\text{m}$, we could reconstruct the 3D chemical distributions of individual aerosol particles from multiple 2D images, as shown in Figure 3. From the 21 SRS images carrying the depth information of a synthetic particle composed of nitrates and sulfates (Figure 3a and Figure S3a, Supporting Information), a 3D structure was rendered by Mimics software (Materialise) and shown in Figure 3b and Movie S1 (Supporting

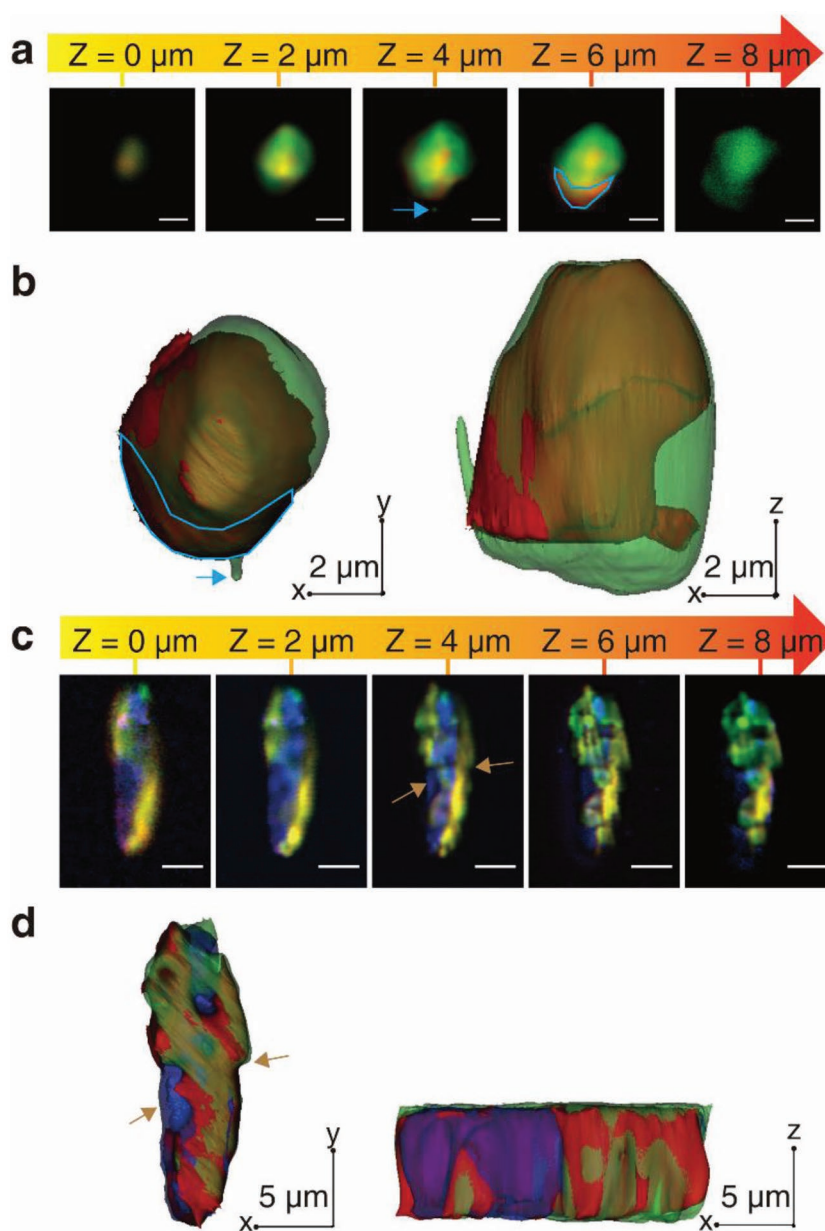


Figure 3. 3D SRS imaging of individual synthetic particles. a) SRS images of a two-component particle taken at selected depths; b) 3D rendered structure of the particle with the distribution of nitrate (green) and sulfate (red), arrows and border lines are used to indicate the corresponding features between (a) and (b); c) SRS images of a three-component particle taken at different depth, d) its 3D rendered structure with nitrate (green), sulfate (red), and oxalate (blue), arrows mark the features of the particle. Scale bar: $1 \mu\text{m}$ in (a) and (b) and $5 \mu\text{m}$ in (c) and (d). Acquisition time: ≈ 42 s for (b) and (d).

Information). The blue arrows and borders marked in Figure 3a,b validate the accuracy of the 3D reconstruction. From the 3D result, we can see that sulfate usually concentrates in the central part of the particle, while nitrate extends more to the peripheral. We can also see that NO_3^- and SO_4^{2-} overlapped at the core as colored yellow, indicating the mutual growth of the two components during the synthetic process. Such conclusions may not be drawn correctly if we only looked at a certain 2D cross section in Figure 3a or Figure S3a

(Supporting Information). Therefore, 3D imaging of aerosol particles is critically important for the accurate measurements of their chemical distributions. Furthermore, we extended our study to image synthesized aerosol particles with three compositions: nitrate (green), sulfate (red), and oxalate (blue), and showed the results of a representative particle in Figure 3c,d. It can be seen that these three-component particles exhibit more complex and irregular distributions than the dual-component ones, implying that the presence of organic component may affect the structures and mixing states of aerosol particles.^[22] With the preknowledge of distinct spectral identities of the major chemical compositions (Figure 1c), SRS microscopy could in principle capture the 3D distributions of all these chemical components within individual particles.

2.4. High-Throughput and Nondestructive Quantification via Large-Scale SRS Imaging

Quantifying chemical compositions of aerosol particles is an essential component in studying their properties and is traditionally done with IC, which requires time-consuming sample preparations. We hypothesized that large-scale SRS imaging allows nondestructive assessment of the overall ratio between various chemical compositions. Previous works have demonstrated the capability of SRS in chemical quantification for biological systems, making use of the linear relationship between SRS signals and chemical concentrations.^[18d,21] To evaluate such ability of SRS for aerosol specimens, we synthesized five samples with different mass ratio of NO_3^- and SO_4^{2-} (N/S), $m_{\text{NO}_3^-} : m_{\text{SO}_4^{2-}} = 1:3, 1:2, 1:1, 2:1, \text{ and } 3:1$. Large-scale SRS images

were taken by mosaic tiling and stitching, and could achieve sample area as large as a few cm^2 . Figure 4a–e shows the results of simulated particles spreading over $\approx 1 \text{ mm} \times 1 \text{ mm}$ area. The mean SRS signal intensities of NO_3^- and SO_4^{2-} were extracted to represent the content of each component, with detailed method described in Notes S2 and S3 (Supporting Information). Meanwhile, the corresponding sample solutions were tested using IC as references. The mass ratios of NO_3^- and SO_4^{2-} were measured with both SRS and IC, and plotted in Figure 4f. The high correlation between the two methods suggests that the mean SRS intensity could serve as a reliable parameter for evaluating the relative abundances of the chemical compositions in aerosol samples. Such a nondestructive method is particularly suited for preliminary measurements, keeping the intact aerosols for further analysis.

We then performed quantitative and statistical analysis for ambient atmospheric aerosols with SRS imaging. The traditional way to analyze particle compositions involves the use of MRS to collect Raman spectra for each particle and assign the Raman peaks to the corresponding chemicals from spectral databases. However, as we have shown above, MRS is incompatible with high-throughput tasks for statistical quantifications due to the substantial time cost. In contrast, SRS hyperspectral imaging is capable of simultaneously acquiring spectral information of all particles within the FOV, providing rapid differentiation of chemical differences between particles. Figure 5a shows an example of an SRS image of atmospheric particles, and the corresponding hyperspectral images could be found in Movie S2 (Supporting Information). As the target Raman frequency varies along the image sequence (850 to 1100 cm^{-1}), we can immediately identify three major

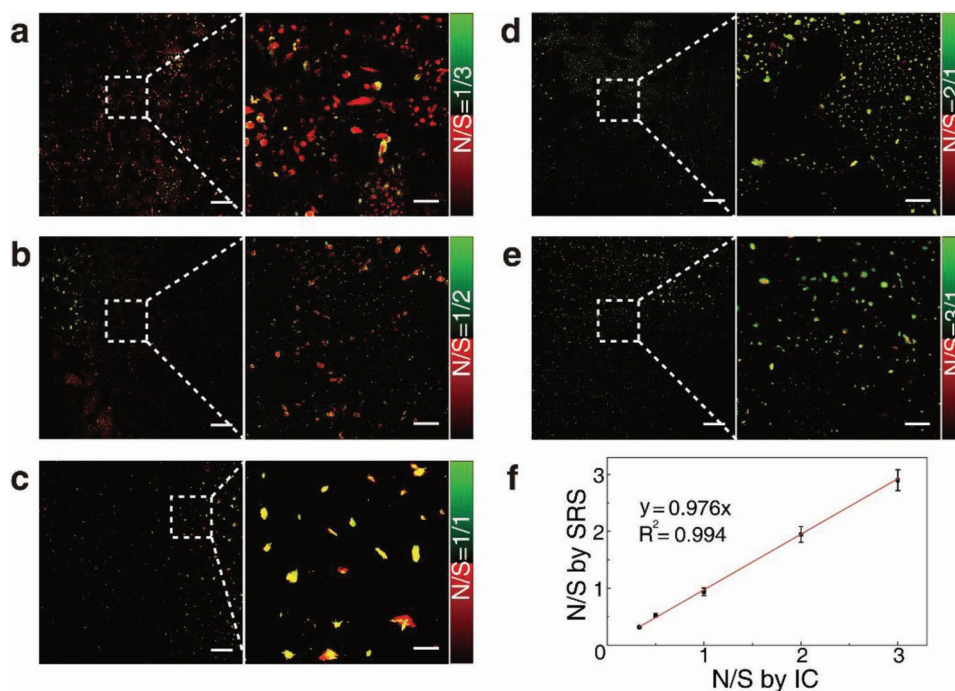


Figure 4. Chemical quantification with SRS imaging. a–e) Stitched SRS image of particles synthesized with different N/S mass ratio (Green: NO_3^- , Red: SO_4^{2-}); f) correlation of measured N/S ratio by SRS and IC. Error bars represent standard error of the mean of three independent measurements. Scale bars: $100 \mu\text{m}$ in zoomed-out images (left) and $20 \mu\text{m}$ in zoomed-in images (right).

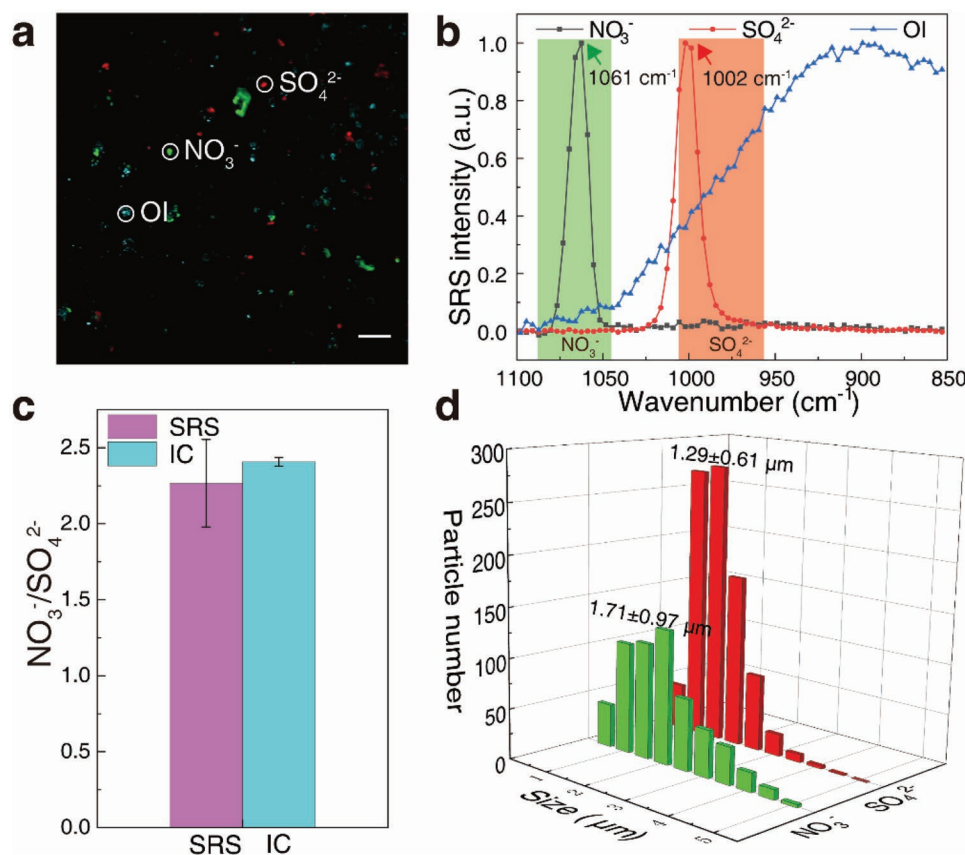


Figure 5. Analysis of atmospheric aerosols with large-area SRS imaging. a) A typical multicolor SRS FOV of atmospheric particles with the distribution of sulfate (red), nitrate (green), and others (blue); b) SRS spectra of the three aerosols circled in (a), shadows indicate the spectral range of NO_3^- and SO_4^{2-} ; c) comparison of SRS and IC quantification for the ratio of NO_3^- to SO_4^{2-} within $\approx 1 \text{ mm} \times 1 \text{ mm}$ area; d) particle size distributions for nitrates and sulfates analyzed from ≈ 1300 particles based on large-area SRS imaging. Scale bar: $20 \mu\text{m}$. Error bars represent standard error of the mean of three independent tests.

types of particles: nitrates, sulfates, and other ingredients (termed as “OI”). Three representative particles are circled in Figure 5a with their spectra shown in Figure 5b. Similar to synthetic particles, nitrate-rich atmospheric particles light up at the Raman shifts around 1060 cm^{-1} , and sulfate-rich particles light up at around 1000 cm^{-1} . However, unlike synthetic particles, atmospheric aerosols contain certain amount of “OI” particles with broad spectral feature of transient absorption (Figure 5b) due to the contaminations of absorptive compounds such as black carbon.^[23] OI appears persistent brightness in the spectral imaging data, whereas nitrates and sulfates particles exhibit sharp resonant behavior as they “blink” during the spectral scan (see Movie S2, Supporting Information). It is worth mentioning that Raman peaks of nitrates and sulfates tend to shift slightly because of the effect of cations, as shown in Figure S4 (Supporting Information) and the literature.^[16c,24] The peaks appearing between 960 and 1005 cm^{-1} are usually classified to be SO_4^{2-} , while those falling in the range of 1045 to 1085 cm^{-1} are considered as NO_3^- .^[24a] Certain organic components could also be detected in the atmospheric particles. The peaks at 1649 and 1678 cm^{-1} in Figure S2 (Supporting Information) may originate from the stretching mode of $\text{C}=\text{O}$ (1610 – 1650 cm^{-1}) or $\text{RO}-\text{NO}_2$ symmetric stretching (organonitrate, $\approx 1653 \text{ cm}^{-1}$) in SOA particles.^[16c,24b] Meanwhile, N/S ratio

of samples was calculated to be 2.27 ± 0.29 based on the large-scale SRS images, in qualitative agreement with IC result of 2.41 ± 0.03 (Figure 5c), indicating the feasibility of SRS quantification method. Besides, large-scale SRS images contain large amount of particles that allow the statistical analysis of particle size distributions for different chemical compositions, as shown in Figure 5d. Comparing with traditional methods for particle number counting and size distributions such as bright-field microscopy and dynamic light scattering (DLS),^[24a,25] SRS provides chemical selective statistics of particles, which could not be easily achieved with traditional means.

2.5. Single-Particle Quantifications of Ambient Atmospheric Aerosols

While statistical results provide ensemble properties of aerosol specimens, single-particle measurements reveal much more detailed structural and chemical information of individual particles, as well as the variations among them. SRS microscopy is able to rapidly search particles of interest based on their spectral and morphological features, followed by zooming-in and tomographic scanning to perform 3D imaging of selected particles, as shown in Figure S5 and Movie S3 (Supporting

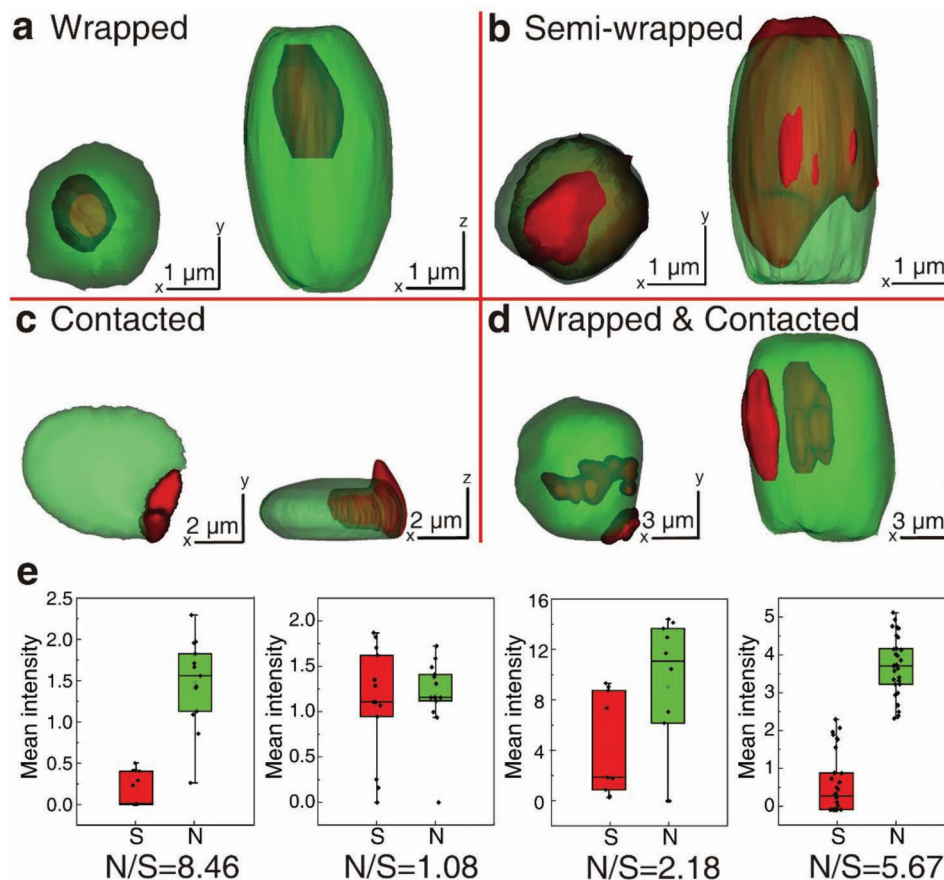


Figure 6. Mixing states and chemical quantification of individual atmospheric aerosol particles. a–d) Different mixing states of individual atmospheric aerosol particles revealed by 3D SRS imaging (Green: NO_3^- , Red: SO_4^{2-}); e) quantification of N/S of individual particles, box and whisker plot showing the distribution of N/S ratio for all image sections. Scale bar: 1 μm in (a) and (b), 2 μm in (c), and 3 μm in (d). Acquisition time: ≈ 26 s for (a) and (b), ≈ 20 s for (c), ≈ 60 s for (d).

Information). With these technological advantages, we captured many single-particle structures and divided them into several types of mixing states, as shown in **Figure 6**. Here, we mainly focused on the particles composed of nitrates and sulfates. In **Figure 6a,b**, sulfates are either completely wrapped or partially wrapped by nitrates. **Figure 6c** represents a typical “contacted” structure where the two components simply adhere to each other. And **Figure 6d** demonstrates a complex structure with both wrapped and contacted sulfates with respect to nitrates. Complete z-stacks are provided in **Figure S6** (Supporting Information) and the 3D rotation animations could be found in **Movie S4** (Supporting Information). Careful examination of these results indicates that the two chemical components are usually spatially isolated in the core of the particles, indicating that sulfate core nucleation occurs prior to nitrate shell deposition (**Figure S6a**, Supporting Information), although in some cases sulfates continue to grow and mix with nitrates (**Figure S6b**, Supporting Information). This phenomenon differs from that of the synthetic particles, in which the two components are spatially overlapped because of the synthetic procedure through nebulizing mixed solution (**Figure S3a**, Supporting Information). These 3D results generate direct visualization of the chemical distributions of single particles,

providing strong evidences for the formation mechanisms of ambient atmospheric aerosols. In addition, chemical quantifications on the single-particle basis could be realized based on the SRS intensity distributions. We calculated N/S ratios of the four typical particles and the results are shown in **Figure 6e**. With the mean SRS intensity of NO_3^- and SO_4^{2-} at each depth section expressed by the box and whisker plot, the mean values of all sections were employed to extract the N/S for each particle. These results indicate that SRS is able to quantify relative contents of the chemical compositions of single atmospheric particles.

3. Discussion

SRS microscopy has been shown as a promising technique for imaging the 3D structures of individual aerosol particles with high spatiotemporal resolution and chemical specificity. Compared with a previous attempt of detecting aerosols with continuous wave (CW) laser based SRS spectroscopy,^[26] modern SRS microscopy has much improved sensitivity and imaging power for single-particle studies. Unlike conceptual models inferred from TEM/EDS and ATOFMS data, the true interior

structures of particles were directly imaged for the first time. 2D images such as those from SEM and TEM lack sufficient information along the z-axis, and are prone to yield inaccurate conclusions. For instance, just focusing on a particular sectional image in Figure S7 (Supporting Information) may infer a spherical particle with a tiny SO_4^{2-} core completely embedded in NO_3^- coating, whereas the full 3D map indicated that SO_4^{2-} was in fact only partially wrapped by NO_3^- . In the current study, we observed that inside ambient aerosol particles nitrates tend to coat sulfates, which is consistent with previous studies that indicated mineral dust particles often contain a $\text{CaSO}_4/\text{K}_2\text{SO}_4$ core coated with $\text{Ca}(\text{NO}_3)_2/\text{Mg}(\text{NO}_3)_2$ due to the heterogeneous reactions of mineral particles and acidic gases.^[3b,15b] Although vibrational spectra of these anions tend to be modulated by different cations as we have shown in Figure S4 (Supporting Information), accurate determination of cation species could not be accomplished only by analyzing Raman spectra (Figure S8, Supporting Information) since other factors such as hydration may also affect the vibrational frequencies of the anions.^[24c,27]

Previous studies have proposed various possible mechanisms and pathways of heterogeneous reactions of NO_x and SO_2 on mineral dust particles using aerosol flow tube methods,^[28] aerosol chamber methods,^[29] SEM/EDS,^[30] and Knudsen cell-mass spectrometer.^[31] Recently, MRS showed promise in obtaining microscopic morphology of particles to understand the reaction mechanisms.^[32] As we have discussed before, the particle structures are related with different heterogeneous reactions. On this basis, SRS microscopy might provide a potential in situ technique for visualizing the dynamical 3D distributions of products in atmospheric heterogeneous reactions with the proper design of microscope-compatible reaction cells and gas circuits, which may provide key evidences for verifying the reaction pathways.

In the field studies of atmospheric inorganic aerosols,^[28a,33] N/S ratio has been widely used as an indicator for relative contribution of mobile to stationary sources of nitrogen and sulfur in the atmosphere. High N/S represents more important contribution of mobile sources than stationary sources of pollutants, and vice versa. SRS quantification for N/S exhibits several advantages over traditional IC, including the high-speed, non-destructiveness, and size distribution analysis. It is conducive to efficient estimation of pollution sources in a real-time detection manner, and thus provides timely regulatory advice for urban pollution control.

However, there are still some technical limitations to widely apply SRS microscopy on single aerosol characterization. First, 3D imaging of aerosol particles in nucleation mode (0–0.1 μm) and condensation mode (0.1–0.56 μm) by SRS are still constrained to a large extent by its diffraction limited spatial resolution of ≈ 350 nm. In addition, quantitative analysis of complex organic components is still not valid enough because of their low concentrations and limited knowledge of standard SRS spectra. Moreover, due to the strong transient absorption background that may overwhelm SRS intensity, black carbon, a significant component of $\text{PM}_{2.5}$, remains difficult for SRS characterization. In the future work, we may achieve a higher spatial resolution (≈ 150 nm) by shortening laser wavelengths,^[34] and obtain more spectral characterization of various organic compounds to further explore the capacity of SRS microscopy

in atmospheric aerosol characterization. Adapting modulation schemes to suppress the background of transient absorption and cross phase modulation may further enable the effective detection of organic compounds in aerosols.^[35] Technical advances to further improve multicolor SRS imaging speed may be incorporated for high-throughput tasks.^[36]

In summary, we have demonstrated for the first time the simultaneous chemical and structural analysis of aerosol particles with SRS microscopy. With its high speed, decent spatial resolution, and 3D chemical imaging capability, SRS presented unique capability in quantifying aerosol compositions at the single-particle level, as well as high-throughput analysis of particle sizes and numbers with chemical specificity. Our method paves a new way for aerosol researches and may shed new light on the formation mechanisms of ambient atmospheric particles.

4. Experimental Section

Sample Preparation: Laboratory-generated aerosol samples were created by nebulizing standard solutions, including the inorganic solution (mixed NaNO_3 and Na_2SO_4) and organic solution (mixed NaNO_3 , Na_2SO_4 , and $\text{C}_3\text{H}_2\text{O}_4\text{Na}_2$). All the chemical agents used in present study were purchased from Sinopharm Chemical Reagent Co. Ltd. At first, air flows out of a compressor and into a two-level air filter system (0.1 and 0.01 μm , respectively) to partially remove impurities. Followed by an air filter (0.01 μm) set to prevent the nebulizer from being contaminated by the remaining impurities. The nebulizer generated aerosol droplets with an aerodynamic. Then aerosol particles were impacted using a microanalysis particle sampler onto coverslips and quartz substrates for SRS and MRS measurements. All samples were kept in a drying cabinet before measurement. Ambient atmospheric aerosols particles were collected on the roof of Environmental Science Building (about 40 m high) at Fudan University (Jianguan Campus, 121°30'E, 31°20'N) on October 24th, 2018. The real-time $\text{PM}_{2.5}$ index was 89 (data were provided by Shanghai Meteorological Bureau). All the samples were collected on quartz membrane filters (QMF) for 12 h using Seven-Stage Non-Viable Andersen Cascade Impactor. Sample-containing filters were stored in a freezer below -10 °C before analysis.

Spontaneous Raman Measurements: MRS of samples was recorded by using a XploRA Plus confocal spectrometer (Jobin Yvon, Horiba Gr, France). Raman scattering was generated by a diode pumped solid-state laser (532 nm) and coupled with a 50 \times Olympus microscope objective (Olympus LMPLFLN50x, NA 0.50). The power of the laser was posed equal to 10% of the maximum power (90 mW). The spectral resolution was 1 cm^{-1} over the range of 100–2000 cm^{-1} . To get 2D spatial distribution of particles, Raman mapping procedure automatically recorded 900 spectra in a $9 \times 9 \mu\text{m}^2$ with 0.3 μm as the minimum step. Every spectrum was obtained by averaging two accumulations with 5 s per acquisition.

Ion Analysis: The ambient samples on QMF were analyzed by IC. 10 mL ultrapure water (specific resistance ≥ 18.2 M Ω cm) was used as the extraction solvent. After 30 min oscillation, the extracted solution was passed through a 0.22 μm PTFE membrane filter and the leaching solution was analyzed using a Metrohm 883 Basic IC equipped with a Metrohm A5-250 column. A weak base eluent (3.2 mmol L⁻¹ Na_2CO_3 plus 1.0 mmol L⁻¹ NaHCO_3) was used for anion detection at a flow rate of 0.70 mL min⁻¹.

SRS Microscopy: In the SRS microscope setup illustrated in Figure S1a (Supporting Information), pulsed femtosecond laser beams from a commercial optical parametric oscillator (OPO) laser (Insight DS+, Newport, CA) were used as the laser source. The fixed fundamental 1040 nm laser was used as the Stokes beam, while the tunable OPO output (680–1300 nm) served as the pump beam. Chirped by SF57 glass

rods, pulse durations of the pump and Stokes beams were stretched to several picoseconds. The intensity of the 1040 nm beam was modulated at 1/4 of the laser pulse repetition rate ($f_0 = 80$ MHz) using a polarizing beam splitter (PBS) and an electrooptical modulator (EOM). The two laser beams were combined through a dichromic mirror (DM), spatially and temporally overlapped, delivered into the laser scanning microscope (FV 1200, Olympus). A 60 \times immersion objective lens (Olympus, UPLSAPO 60XWIR, NA 1.2 water) was utilized to focus the light into the sample. The simulated Raman loss (SRL) signal was optically filtered (CARS ET890/220, Chroma), detected by a homemade back-biased photodiode (PD) and demodulated with a lock-in amplifier (LIA) (HF2LI, Zurich Instruments) to feed the analog input of the microscope to form images. The SRS spectra could be acquired by scanning the optical delay line of a motorized translation stage (M-ILS250CC, Newport) and further calibration of wavenumber and delay line is detailed in Figure S1b,c (Supporting Information). A typical SRS image takes ≈ 1 s, with 2 μ s pixel dwell time, and image size of 512 \times 512 pixels. The laser powers of 20 mW of pump and 30 mW for Stokes pulses were used at samples. All images were taken in transmission mode.

Supporting Information

Supporting Information is available from the Wiley Online Library or from the author.

Acknowledgements

J.A. and Y.F. contributed equally to this work. The authors thank the financial support from the National Natural Science Foundation of China (81671725, 21677037, and 61975033); Shanghai Municipal Science and Technology Major Project (2017SHZDZX01); National Key R&D Program of China (2016YFA0301000); and Specialized Research Project of the Shanghai Health and Family Planning Commission on Smart Medicine (2018ZHYL0204).

Conflict of Interest

The authors declare no conflict of interest.

Keywords

3D chemical imaging, atmospheric particles, hyperspectral imaging, single particle analysis, stimulated Raman scattering microscopy

Received: August 29, 2019
Revised: November 12, 2019
Published online: December 11, 2019

- [1] a) A. P. Ault, J. L. Axson, *Anal. Chem.* **2017**, *89*, 430; b) K. Li, J. Li, J. Liggio, W. Wang, M. Ge, Q. Liu, Y. Guo, S. Tong, J. Li, C. Peng, B. Jing, D. Wang, P. Fu, *Environ. Sci. Technol.* **2017**, *51*, 1285.
- [2] E. Underwood, *Science* **2017**, *355*, 342.
- [3] a) R. C. Moffet, K. A. Prather, *Proc. Natl. Acad. Sci. USA* **2009**, *106*, 11872; b) W. Li, J. Sun, L. Xu, Z. Shi, N. Riemer, Y. Sun, P. Fu, J. Zhang, Y. Lin, X. Wang, L. Shao, J. Chen, X. Zhang, Z. Wang, W. Wang, *J. Geophys. Res.: Atmos.* **2016**, *121*, 13.
- [4] C. Li, Q. He, J. Schade, J. Passig, R. Zimmermann, D. Meidan, A. Laskin, Y. Rudich, *Atmos. Chem. Phys.* **2019**, *19*, 139.
- [5] H. D. Lee, A. D. Estillore, H. S. Morris, K. K. Ray, A. Alejandro, V. H. Grassian, A. V. Tivanski, *J. Phys. Chem. A* **2017**, *121*, 8296.
- [6] J. M. Conny, R. D. Willis, D. L. Ortiz-Montalvo, *J. Geophys. Res.: Atmos.* **2019**, *124*, 2702.
- [7] L. Xu, D. Zhang, W. Li, *Sci. Total Environ.* **2019**, *669*, 948.
- [8] a) A. Kalume, C. Wang, J. Santarpia, Y.-L. Pan, *Chem. Phys. Lett.* **2018**, *706*, 255; b) A. L. Bondy, R. M. Kirpes, R. L. Merzel, K. A. Pratt, M. M. B. Holl, A. P. Ault, *Anal. Chem.* **2017**, *89*, 8594.
- [9] a) B. H. Lee, F. D. Lopez-Hilfiker, P. R. Veres, E. E. McDuffie, D. L. Fibiger, T. L. Sparks, C. J. Ebben, J. R. Green, J. C. Schroder, P. Campuzano-Jost, S. Iyer, E. L. D'Ambro, S. Schobesberger, S. S. Brown, P. J. Wooldridge, R. C. Cohen, M. N. Fiddler, S. Bililign, J. L. Jimenez, T. Kurten, A. J. Weinheimer, L. Jaegle, J. A. Thornton, *J. Geophys. Res.: Atmos.* **2018**, *123*, 7670; b) L. Shen, H. Wang, Y. Yin, J. Chen, K. Chen, *Atmos. Environ.* **2019**, *201*, 148; c) S. Ghosal, P. K. Weber, A. Laskin, *Anal. Methods* **2014**, *6*, 2444.
- [10] L. Wu, X. Li, H. Kim, H. Geng, R. H. M. Godoi, C. G. G. Barbosa, A. F. L. Godoi, C. I. Yamamoto, R. A. F. de Souza, C. Poehlker, M. O. Andreae, C.-U. Ro, *Atmos. Chem. Phys.* **2019**, *19*, 1221.
- [11] a) S. Smith, M. Ward, R. Lin, R. Brydson, M. Dall'Osto, R. M. Harrison, *Atmos. Environ.* **2012**, *62*, 400; b) E. Freney, K. Sellegri, M. Chrit, K. Adachi, J. Brito, A. Waked, A. Borbon, A. Colomb, R. Dupuy, J.-M. Pichon, L. Bouvier, C. Delon, C. Jambert, P. Durand, T. Bourianne, C. Gaimoz, S. Triquet, A. Feron, M. Beekmann, F. Dulac, K. Sartelet, *Atmos. Chem. Phys.* **2018**, *18*, 7041.
- [12] Z. Dong, D. Qin, K. Li, S. Kang, T. Wei, J. Lu, *Environ. Pollut.* **2019**, *246*, 79.
- [13] J. Ofner, T. Deckert-Gaudig, K. A. Kamilli, A. Held, H. Lohninger, V. Deckert, B. Lendl, *Anal. Chem.* **2016**, *88*, 9766.
- [14] a) D. Gupta, H. J. Eom, H. R. Cho, C. U. Ro, *Atmos. Chem. Phys.* **2015**, *15*, 11273; b) R. L. Craig, L. Nandy, J. L. Axson, C. S. Dutcher, A. P. Ault, *J. Phys. Chem. A* **2017**, *121*, 5690; c) H.-J. Eom, D. Gupta, H.-R. Cho, H. J. Hwang, S. D. Hur, Y. Gim, C.-U. Ro, *Atmos. Chem. Phys.* **2016**, *16*, 13823.
- [15] a) Y. Batonneau, S. Sobanska, J. Laureyns, C. Bremard, *Environ. Sci. Technol.* **2006**, *40*, 1300; b) S. Sobanska, H. Hwang, M. Choel, H. J. Jung, H. J. Eom, H. Kim, J. Barbillat, C. U. Ro, *Anal. Chem.* **2012**, *84*, 3145.
- [16] a) M. Gen, C. K. Chan, *Atmos. Chem. Phys.* **2017**, *17*, 14025; b) Y. Fu, C. Kuppe, V. K. Valev, H. Fu, L. Zhang, J. Chen, *Environ. Sci. Technol.* **2017**, *51*, 6260; c) R. L. Craig, A. L. Bondy, A. P. Ault, *Anal. Chem.* **2015**, *87*, 7510.
- [17] a) C. W. Freudiger, W. Min, B. G. Saar, S. Lu, G. R. Holtom, C. He, J. C. Tsai, J. X. Kang, X. S. Xie, *Science* **2008**, *322*, 1857; b) P. Nandakumar, A. Kovalev, A. Volkmer, *New J. Phys.* **2009**, *11*, 033026; c) W. Min, C. W. Freudiger, S. Lu, X. S. Xie, *Annu. Rev. Phys. Chem.* **2011**, *62*, 507.
- [18] a) J. X. Cheng, X. S. Xie, *Science* **2015**, *350*, aaa8870; b) M. Ji, M. Arbel, L. Zhang, C. W. Freudiger, S. S. Hou, D. Lin, X. Yang, B. J. Bacskai, X. S. Xie, *Sci. Adv.* **2018**, *4*, eaat7715; c) M. Ji, D. A. Orringer, C. W. Freudiger, S. Ramkissoon, X. Liu, D. Lau, A. J. Golby, I. Norton, M. Hayashi, N. Y. Agar, G. S. Young, C. Spino, S. Santagata, S. Camelo-Piragua, K. L. Ligon, O. Sagher, X. S. Xie, *Sci. Transl. Med.* **2013**, *5*, 201ra119; d) M. C. Wang, W. Min, C. W. Freudiger, G. Ruvkun, X. S. Xie, *Nat. Methods* **2011**, *8*, 135; e) F. Tian, W. Yang, D. A. Mordas, J. Y. Wang, J. S. Salameh, J. Mok, J. Chew, A. Sharma, E. Leno-Duran, S. Suzuki-Uematsu, N. Suzuki, S. S. Han, F. K. Lu, M. Ji, R. Zhang, Y. Liu, J. Strominger, N. A. Shneider, L. Petrucelli, X. S. Xie, K. Eggan, *Nat. Commun.* **2016**, *7*, 13283.
- [19] a) Q. Cheng, L. Wei, Z. Liu, N. Ni, Z. Sang, B. Zhu, W. Xu, M. Chen, Y. Miao, L. Q. Chen, W. Min, Y. Yang, *Nat. Commun.* **2018**, *9*, 2942; b) M.-A. Houle, R. C. Burruss, A. Ridsdale, D. J. Moffatt, F. Légaré, A. Stolow, *J. Raman Spectrosc.* **2017**, *48*, 726.

- [20] M. C. Fischer, J. W. Wilson, F. E. Robles, W. S. Warren, *Rev. Sci. Instrum.* **2016**, *87*, 031101.
- [21] a) A. Gupta, G. F. Dorlhiac, A. M. Streets, *Analyst* **2019**, *144*, 753; b) X. Li, Y. Li, M. Jjiang, W. Wu, S. He, C. Chen, Z. Qin, B. Z. Tang, H. Y. Mak, J. Y. Qu, *Anal. Chem.* **2019**, *91*, 2279; c) D. Fu, J. Zhou, W. S. Zhu, P. W. Manley, Y. K. Wang, T. Hood, A. Wylie, X. S. Xie, *Nat. Chem.* **2014**, *6*, 614.
- [22] a) C. N. Cruz, S. N. Pandis, *J. Geophys. Res.: Atmos.* **1998**, *103*, 13111; b) R. Zhang, I. Suh, J. Zhao, D. Zhang, E. C. Fortner, X. Tie, L. T. Molina, M. J. Molina, *Science* **2004**, *304*, 1487.
- [23] L. Zhang, S. Shen, Z. Liu, M. Ji, *Adv. Biosyst.* **2017**, *1*, 1700013.
- [24] a) Z. Sun, F. Duan, K. He, J. Du, L. Yang, H. Li, T. Ma, S. Yang, *J. Environ. Sci.* **2019**, *75*, 388; b) Q. X. Ma, H. He, C. Liu, *Atmos. Environ.* **2013**, *69*, 281; c) H. Morillas, I. Marcaida, C. Garcia-Florentino, M. Maguregui, G. Arana, J. M. Madariaga, *Sci. Total Environ.* **2018**, *615*, 691.
- [25] R. P. Singh, V. K. Jaiswal, V. K. Jain, *Appl. Opt.* **2006**, *45*, 2217.
- [26] K. H. Fung, D. G. Imre, I. N. Tang, *J. Aerosol Sci.* **1994**, *25*, 479.
- [27] M. Ji, S. Park, K. J. Gaffney, *J. Phys. Chem. Lett.* **2010**, *1*, 1771.
- [28] a) X. X. Ding, L. D. Kong, C. T. Du, A. Zhanzakova, H. B. Fu, X. F. Tang, L. Wang, X. Yang, J. M. Chen, T. T. Cheng, *Atmos. Environ.* **2017**, *167*, 625; b) Y. Zhao, Y. C. Liu, J. Z. Ma, Q. X. Ma, H. He, *Atmos. Environ.* **2017**, *152*, 465.
- [29] a) K. W. Li, L. H. Chen, K. Han, B. A. Lv, K. J. Bao, X. C. Wu, X. Gao, K. F. Cen, *Atmos. Res.* **2017**, *184*, 139; b) J. Park, M. Jang, Z. C. Yu, *Environ. Sci. Technol.* **2017**, *51*, 9605; c) Z. C. Yu, M. Jang, *Atmos. Chem. Phys.* **2018**, *18*, 14609.
- [30] W. J. Li, L. Y. Shao, *Aerosol Air Qual. Res.* **2012**, *12*, 1095.
- [31] Q. X. Ma, Y. C. Liu, C. Liu, J. Z. Ma, H. He, *J. Environ. Sci.* **2012**, *24*, 62.
- [32] D. Zhao, S. H. Schmitt, M. Wang, I.-H. Acir, R. Tillmann, Z. Tan, A. Novelli, H. Fuchs, I. Pullinen, R. Wegener, F. Rohrer, J. Wildt, A. Kiendler-Scharr, A. Wahner, T. F. Mentel, *Atmos. Chem. Phys.* **2018**, *18*, 1611.
- [33] a) X. H. Yao, C. K. Chan, M. Fang, S. Cadle, T. Chan, P. Mulawa, K. B. He, B. M. Ye, *Atmos. Environ.* **2002**, *36*, 4223; b) Y. Wang, G. Zhuang, X. Zhang, K. Huang, C. Xu, A. Tang, J. Chen, Z. An, *Atmos. Environ.* **2006**, *40*, 2935; c) Y. Tao, X. Ye, Z. Ma, Y. Xie, R. Wang, J. Chen, X. Yang, S. Jiang, *Atmos. Environ.* **2016**, *145*, 1.
- [34] Y. Bi, C. Yang, Y. Chen, S. Yan, G. Yang, Y. Wu, G. Zhang, P. Wang, *Light: Sci. Appl.* **2018**, *7*, 81.
- [35] a) P. Berto, E. R. Andresen, H. Rigneault, *Phys. Rev. Lett.* **2014**, *112*, 053905; b) D. Zhang, M. N. Slipchenko, D. E. Leaird, A. M. Weiner, J. X. Cheng, *Opt. Express* **2013**, *21*, 13864.
- [36] a) R. He, Y. Xu, L. Zhang, S. Ma, X. Wang, D. Ye, M. Ji, *Optica* **2017**, *4*, 44; b) B. Zhang, M. Sun, Y. Yang, L. Chen, X. Zou, T. Yang, Y. Hua, M. Ji, *Biomed. Opt. Express* **2018**, *9*, 2604.